ACS APPLIED MATERIALS & INTERFACES

www.acsami.org

Research Article

Pressure-Based Immunoassays with Versatile Electronic Sensors for Carcinoembryonic Antigen Detection

Lingting Huang, Yongyi Zeng, Xiaolong Liu, and Dianping Tang*

Cite This: *ACS Appl. Mater. Interfaces* 2021, 13, 46440–46450

Read Online

ACCESS | Metrics & More | Article Recommendations | Supporting Information

ABSTRACT: Pressure-based immunoassays have been studied for point-of-care testing for which increasing the sensitivity is still a challenge. In this study, we described an enhanced pressure-based immunoassay with a versatile electronic sensor for the sensitive biological analysis. The versatile electronic sensor had multifunctional sensing capabilities with temperature and pressure recording. Magnetic bead-modified capture antibody and platinum nanoparticle-labeled detection antibody were used as the biorecognition element of the target carcinoembryonic antigen (CEA) (as a model analyte) and would form a sandwich-type immune complex with CEA. After simple magnetic separation, this complex was transferred into the detection chamber, which contained both hydrogen peroxide (H_2O_2) and 3,3′,5,5′-tetramethylbenzidine (TMB). With the catalytic ability of PtNPs, the "H_2O_2−TMB−PtNPs" system was catalyzed to generate a large amount of oxygen (O_2) and photothermal agent of oxidizer TMB (ox-TMB). Meanwhile, in a sealed chamber, further irradiation with an 808 nm near-infrared laser led to a triple-step signal amplification strategy of pressure increase, temperature increase, and gas thermal expansion to receive a strong electrical signal through the electronic sensor in real time. Thus, the amplified electrical signal from the electronic sensor could reveal the target concentration. In addition, we also verified that the synergistic system with two physical quantities had a lower limit of detection and a wider detection range compared to the detection system with a single physical quantity. In general, this immunoassay not only helped in exploring an effective signal amplification pathway but also offered an opportunity for the development of versatile electronic sensors in point-of-care settings.

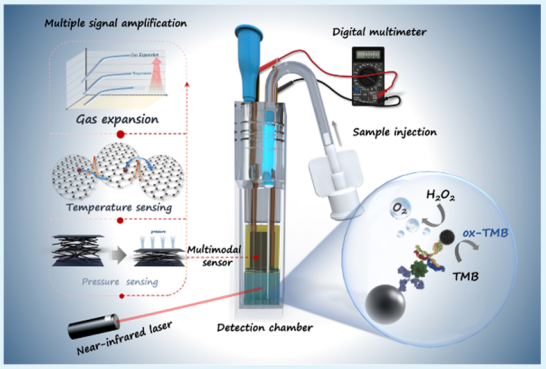

KEYWORDS: *versatile electronic sensor, multimodal, point-of-care testing, pressure-based immunoassay, carcinoembryonic antigen*

1. INTRODUCTION

The sensitive detection of tumor markers in biological fluids occupies an extremely important position in the clinical diagnosis and prognosis.[1,2] Although some conventional immunoassays are usually sufficient to achieve highly sensitive and selective clinical trials, it is inevitable that with the rapid advancement of medicine and the ever-faster pace of people's lives, quick on-site tests are very attractive without large instruments and complex operations.[3,4] Point-of-care testing (POCT) generally refers to rapid detection and analysis techniques used in places other than the laboratory to get instant detection results, such as accident sites, sampling points, and homes.[5,6] Relying on the advantages of speed and convenience coupled with the constant emergence of new technologies, POCT has taken a new direction for rapid development in the field of in vitro diagnostics.[5,7] In general, POCT with excellent performance must have an effective signal transmission path to bridge the gap between biological detection and signal readout. The general physical signal conversion methods mostly convert the concentration of the detected target into physical signals such as color, mass, temperature, pressure, electrochemistry, and volume change.[7−12] Among them, air pressure as a classic physical quantity has been applied in POCT. In 2014, Yang et al. pioneered to use air pressure changes as the detection signal for sensitive biomedical analysis with a portable pressure meter.[13] Hence, this has inspired many researchers to conduct extensive studies in the fields of pressure-based bioassays using various pressure sensors in the detection of biomolecules.[14−16]

Although the application of pressure sensors in biological analytics has started to shine, research to further improve the sensitivity is still worth exploring. So far, the pressure sensor in the pressure-based bioassay was mostly used as a single-function sensor that only aimed at the physical size of air pressure. Encouragingly, to meet a wider range of detection

Received: August 28, 2021
Accepted: September 14, 2021
Published: September 22, 2021

https://doi.org/10.1021/acsami.1c16514
ACS Appl. Mater. Interfaces 2021, 13, 46440−46450

Scheme 1. (A) Sandwich-Type Immunoreaction and Catalytic Reactions of the Detection System and (B) Schematic Illustration of Enhanced Pressure-Based Immunoassay Based on the Versatile Electronic Sensor Readout for the Detection of CEA

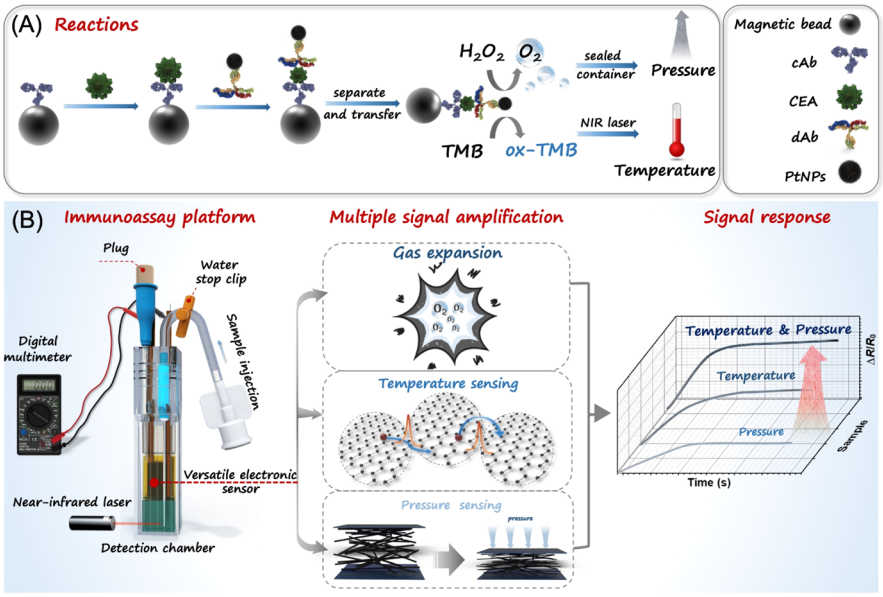

requirements, versatile electronic sensors that can realize multimodal sensing have gained increasing development.[17−19] Just like a general electronic sensor, the multimodal sensor usually consists of two parts: a conductive material (such as carbon-based materials,[20−22] conductive polymer-based materials,[23−25] and metals[26−28]) and a flexible bracket component [such as sponges,[23,29] polydimethylsiloxane (PDMS),[24,26,30] papers,[28,31] and fabric[32−34]] with mechanical matching characteristics, but they can realize the simultaneous output of multiple signals. Various physical quantities of temperature, pressure, stress, and humidity can be converted into coupling signals by versatile electronic sensors.[17,35−37] The advent of versatile electronic sensors extends the detection strategy of pressure-based biological analysis by breaking the limitation of the detection mode to a single physical quantity, and it is expected that better detection performance will be achieved under the synergistic effect of multiple physical quantities.

As we all know, many physical stimuli, such as electrical resistance, volume expansion, vapor pressure, and spectral characteristics are related to temperature. There is a type of temperature-sensitive conductor that has a temperature-dependent resistance.[38−40] The temperature coefficient of resistance (TCR) can be used to describe this temperature-sensitive behavior intuitively, as defined by the formula of TCR = $(R_T - R_0)/R_0 \times \Delta T$, (where R_0, R_T, and ΔT are the initial resistance at the beginning, the resistance at the set temperature, and the temperature change, respectively), which corresponds to the relative change in resistance caused by the temperature change of the conductor per degree Celsius.[25,40,41] According to the value of the temperature coefficient, temperature-sensitive conductive materials can be divided into positive temperature coefficient conductors and negative temperature coefficient (NTC) conductors. The characteristic of an NTC conductor is that its resistance decreases linearly/nonlinearly with the increasing temperature.[40,42] Graphene is a semimetal with a zero band gap with unique electrical properties. A considerable number of experiments have verified that the resistance of graphene oxide (GO) decreases with the increasing temperature, indicating an NTC property.[43,44] Having the property of an NTC, reduced graphene oxide (rGO) is widely used due to its higher conductivity than GO.[21,45] In particular, it should be mentioned that piezoresistive pressure sensors are often used as signal transduction media in pressure-based immunoassays. The air pressure generated during the detection process leads to a shift in the position of the conductive material loaded in the framework to move and also causes a change in resistance.[46] Here, we have seen that the application of conductive materials in temperature sensing and pressure sensing is the matching of resistance changes, which is also a prerequisite for the construction of multimodal sensors. At the same time, it also offers us a unique signal amplification strategy for the application of versatile electronic sensors in the analysis of biomolecules.

As a broad-spectrum tumor marker, the carcinoembryonic antigen (CEA) has an important clinical value in the differential diagnosis, disease monitoring, and efficacy assessment of malignant tumors.[47] Therefore, the development of a sensitive, accurate, and low-cost method for the immediate detection of CEA is of great significance for clinical diagnosis and therapy. Against this background, as a proof of concept, we designed a versatile electronic sensor, which consists of a temperature-sensitive conductive material rGO with an NTC property based on cotton fabric as a flexible frame. In a system that simultaneously introduced two physical quantities of temperature and pressure, an enhanced pressure-based immunoassay was constructed to realize high-performance biological detection using CEA as an example. Scheme 1A shows the sandwich-type immunoreaction and catalytic reactions of the detection system. In our design, the magnetic bead-modified capture antibody (MBs-cAb) and the platinum nanoparticle-labeled detection antibody (PtNPs-dAb) are used as the biorecognition element of the target CEA. With the presence of CEA, the target will undergo a biological recognition event with MB-cAb and PtNPs-dAb to form a sandwich-type immune complex. Under the influence of

https://doi.org/10.1021/acsami.1c16514
ACS Appl. Mater. Interfaces 2021, 13, 46440−46450

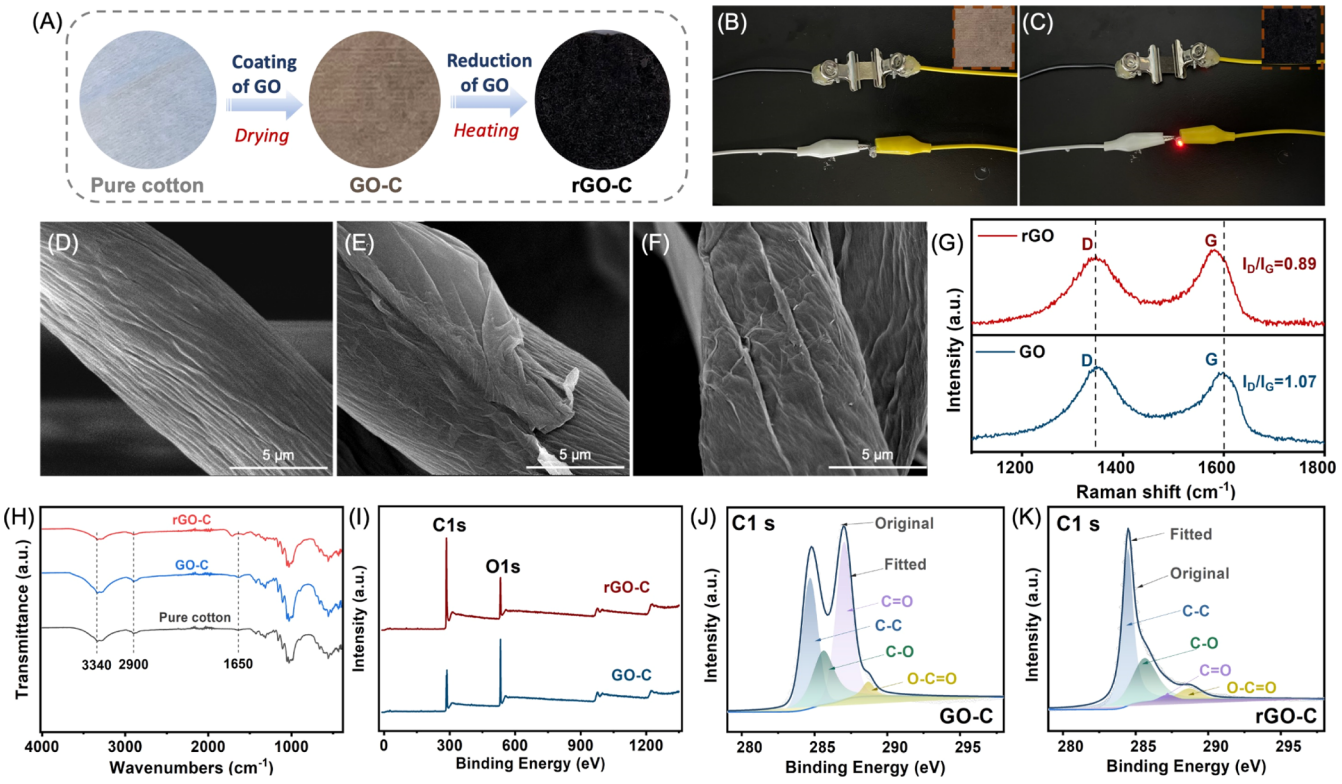

Figure 1. (A) Preparation process of rGO-C. The brightness response of the LED in the circuit connecting with (B) GO-C and (C) rGO-C changes. Scanning electron microscopy (SEM) images of (D) pure cotton fabric, (E) GO-C, and (F) rGO-C. (G) Raman spectra of GO-C and rGO. (H) Fourier transform infrared spectroscopy (FTIR) spectra of pure cotton, GO-C, and rGO-C. (I) X-ray photoelectron spectroscopy (XPS) survey spectrum, and high-resolution XPS spectra of C 1s for (J) GO-C and (K) rGO-C.

external magnetic force, the complex is separated and transferred to a closed detection chamber that contains both hydrogen peroxide (H_2O_2) and 3,3′,5,5′-tetramethylbenzidine (TMB). PtNPs have a double-layer catalytic effect in the "H_2O_2−TMB−PtNPs" system. PtNPs can decompose H_2O_2 to generate a large amount of oxygen (O_2). In addition, PtNPs also have a peroxidase-like catalytic activity that can effectively oxidize TMB into an excellent photothermal oxidation TMB (ox-TMB). With the irradiation of 808 nm near-infrared (NIR) laser, strong increases of pressure and temperature will occur in the closed detection device at the same time. As shown in Scheme 1B, a versatile electronic sensor is further placed in the integrated immunoassay platform. Under the action of air pressure, the contact resistance of the multimodal sensor decreases, which is a typical property of a piezoresistive pressure sensor. At the same time, rGO will further reduce the resistance when the temperature increases due to its NTC thermal sensitivity. Most notably, in a closed container, the role of gas expansion caused by high temperature in synergistic pressure increase cannot be ignored. In general, the purpose of this article is to construct a new strategy to construct a versatile electronic sensor for an enhanced pressure-based immunoassay by means of cooperative signal amplification with multiple physical quantities to meet the needs of the family medical and health care environment.

2. EXPERIMENTAL SECTION

2.1. Preparation of GO-Coated Cotton (GO-C) and rGO-Coated Cotton (rGO-C). GO-C was obtained on the cotton fabric by a simple dipping process. Before covering, the pure cotton fabric was first ultrasonically cleaned for 1 h at 50 °C with 1.0 M NaOH. Next, the GO was prepared by Hummers' method with a slight modification.[48] In order to combine more GO with cotton fabrics, the cleaned cotton fabrics were soaked in GO dispersion for 30 min and then treated by freeze-drying. These operation steps were carried out a total of three times.

Afterward, the cotton fabric soaked with GO was then converted into rGO-coated cotton with good electrical conductivity by a simple thermal reduction treatment. In detail, GO-C was processed in an oven at 200 °C for 2 h to obtain rGO-C.

2.2. Fabrication of Versatile Electronic Sensor and Detection Device. First, the prepared rGO-C was cut into a sample with a size of 1.0 × 0.6 cm^2. Then, silver paste, copper foil tape, and copper wire were attached to each side of rGO-C after cutting (the copper foil tape and the copper wire were connected into a copper foil-copper wire-copper foil sandwich structure, and silver paste was used to connect the sandwich structure into the rGO-C interface). Then, to create a sealed atmosphere, Kapton tape was used to further encapsulate rGO-C, so that it could be isolated from the external environment. It was worth noting that the part of the Kapton tape that would contact with rGO-C was previously rubbed with absorbent cotton in order to remove the stickiness of the tape, to prevent the tape from sticking to the conductive fiber surface, and to reduce the possible irreversibility reduce deformation of the sensor after pressure transmission.

To fabricate an integrated detection device for the immunoassay, a 1.5 mL cuvette cell was used as the detection container. First, one cuvette was used as a mold. The multimodal sensor, the needle, and the injection tube were fixed in a certain position, and then, PDMS was poured into the cuvette and cured at 90 °C for 2 h. After removal from the mold, the lower portion of PDMS was cut flat at 1 × 2 cm^2 to expose the sensor and pinholes, so that the top cover of the PDMS-molded detection device was made. Finally, the top cover and another cuvette cell covered with the thermally conductive layer (1 × 2 cm^2) were assembled. The joint was further sealed with resin, and an

https://doi.org/10.1021/acsami.1c16514
ACS Appl. Mater. Interfaces 2021, 13, 46440−46450

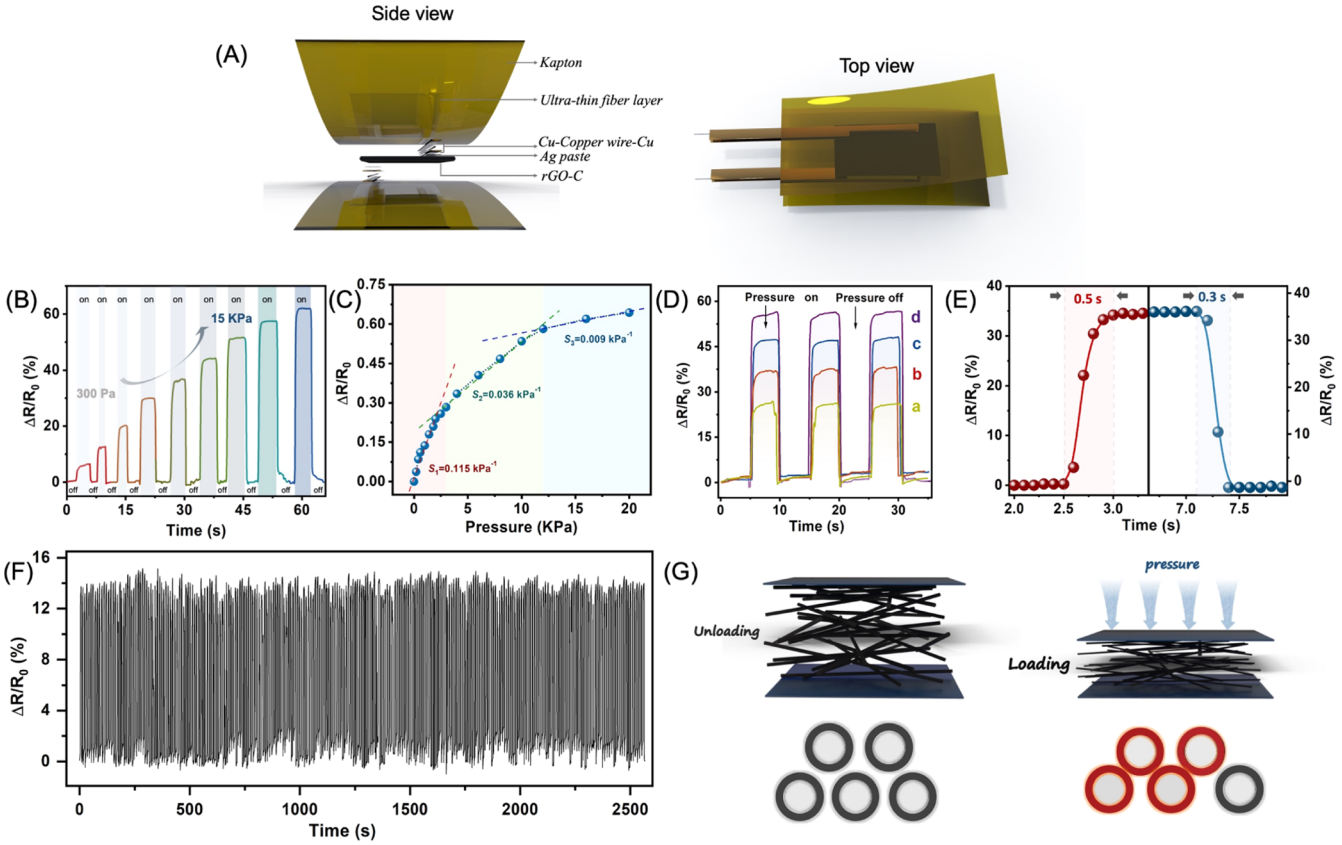

Figure 2. (A) Side and top views of the structural design of the multimodal sensor. (B) Response of the multimodal sensor to different pressures. (C) Sensitivity of the multimodal sensor for pressure sensing. (D) Repeated measurements at different pressures. (E) Response time and recovery time for the pressure detection of the multimodal sensor. (F) Durability test of the sensor for 250 loading−unloading cycles at 1.0 kPa. (G) Sensing mechanism of the multimodal sensor for pressure detecting.

integrated detection device combined with a multimodal sensor was produced (Scheme S1).

3. RESULTS AND DISCUSSION

3.1. Preparation and Characterization of GO-C and RGO-C. GO-C was obtained by a simple dipping process. It could be observed from Figure 1A that the color of the cotton fabric had changed from white to brown after the treatment. GO interacted with the cotton fiber surface through van der Waals forces with low bonding strength. Therefore, a series of dip coating and drying cycles were performed to increase the GO content on the cotton sheet for a better bond. According to the formula, the dip-coating ratio [coating ratio = $(m_p - m_c)/m_p \times 100\%$, where m_p and m_c are the mass of pure cotton fabric and GO-C] was up to 13.4% (Figure S1). To verify the conductivity of GO-C after treatment, GO-C and rGO-C were connected to the circuit of the light-emitting diode (LED) to make the change in resistance visible. GO-C had poor conductivity and could not power the LED (Figure 1B). In contrast, the LED connected to the rGO-C circuit emitted a bright red light (Figure 1C), which meant that the GO loaded on the cotton fabric was converted into a more conductive substance after heat treatment.

Logically, a series of systematic characterizations were performed to further confirm the conversion of GO to rGO. Specifically, SEM, Raman spectroscopy, FTIR, and XPS were used to provide a more complete observation of the material. Initially, SEM was used to observe the morphology of samples before and after treatment. It is worth noting that the freeze-drying method could reduce the filling of conductive GO between the cotton fiber interstices, which was beneficial for the prepared sensor to arrive a more sensitive response to pressure (Figure S2). As shown in Figure 1D, the surface of the cotton fabric was clean and with no observable contamination after washing. The original fabric had a special spiderweb-like structure, and the cotton fibers were tangled together. As depicted in the cross-sectional SEM image (Figure S3), the fabric presented a three-dimensional porous structure with an intricate network. As shown in Figure 1E, the GO adhered to the surface of the cotton fabric and formed a unique wrinkle morphology. This result indicates the successful assembly of GO nanosheets on the cotton fiber. Furthermore, the layered structure and the wrinkled morphology on the fiber surface could still be observed after thermal reduction treatment (Figure 1F). This result was considered to be the uniform coating of the ultrathin and uniform GO nanosheets on the fiber surface.

Raman spectroscopy was also used to characterize the sample. The spectra of GO-C and rGO-C are shown in Figure 1G, which display the existence of the D band of 1347 cm^{-1} and the G band of 1600 cm^{-1}. The D band indicated a defect caused by the presence of oxygen atoms at a large interplanar distance. The stretching motion of the in-plane bond of the E_{2g} phonon of the C sp^2 atoms produces a G band.[49,50] Generally, the intensity ratio of the D band to the G band (I_D/I_G) is viewed as an indicator of a relatively disordered structure.[51] After treatment at 200 °C, the related defects were reduced due to the decrease in the oxygen content, and the I_D/I_G ratio

https://doi.org/10.1021/acsami.1c16514
ACS Appl. Mater. Interfaces 2021, 13, 46440−46450

was reduced from 1.07 (GO-C) to 0.89 (rGO-C). In order to gain a deep understanding of the chemical reactions that occur during the heat treatment, FTIR was used to analyze the changes in the characteristic groups on the surface of different fabrics. As shown in Figure 1H, peaks around 3340, 2900, and 1650 cm^{-1} were observed from the FTIR spectrum of untreated cotton fabric, corresponding to O−H stretching, asymmetric C−H stretching, and stretching of C═O.[52,53] There were no significant changes in the FTIR spectrum of the cotton fabric after the GO impregnation treatment. In contrast, the broadband occurring in the −OH group between 3400 and 3000 cm^{-1} became weaker after heat treatment, which indicated that the hydroxyl group in GO-C was reduced. At the same time, it was found that the peak at 1650 cm^{-1} disappeared and the peak intensity at 2900 and 3340 cm^{-1} decreased significantly, suggesting that most of the GO were reduced to rGO. In addition, XPS was used to further analyze the elements of C, O, and N in GO-C and rGO-C (Figure 1I). The relative contents of C 1s, O 1s, and N 1s are shown in Table S1. It could be seen intuitively that the conversion of GO-C to rGO-C was accompanied by a decrease in the O content and a regular increase in the C content. The O 1s/C 1s content ratios of GO-C and rGO-C were calculated to be 40.56 and 20.71%. The carbon-containing groups on the fabric surface were attributed to C−C (284.7 eV), C−O (285.6 eV), C═O (287.1 eV), and O−C═O (288.7 eV) (Figure 1J,K).[54] The heat treatment caused the strength of C═O to decrease from 43 to 1.9%, while the peak strength of C−C and C−O increased to 56.4 and 35.3%, respectively (Table S2). Furthermore, the morphology characterization of GO and rGO sheets was conducted using SEM, transmission electron microscopy (TEM), and atomic force microscopy (please see Figure S4 and the corresponding description). These results indicate that the heat treatment caused the reduction of GO on the surface of the cotton fabric to rGO.

3.2. Probe into the Performance of Pressure Sensors.

Figure 2A shows the structural design of the multimodal sensor. The prepared sensor with considerable flexibility benefited from the excellent bendability and twist ability of the original pure cotton fabric (Figure S5). The thickness of the sandwich structure sensor was only 0.48 mm (Figure S6), which benefited the construction of an integrated detector.

The pressure responses of the rGO-C-based multimodal sensor under different external conditions were systematically examined to verify the sensing performance of the sensor. The rate of the relative change in resistance [$\Delta R/R_0 = (R_0 - R)/R_0 \times 100\%$, where R_0 is applied to the initial resistance in an unpressurized state and R equals the resistance of the device at a given pressure] was used to determine the pressure response to characterize. The curve of $\Delta R/R_0$ versus time at different pressures is illustrated in Figure 2B. Obviously, the value of $\Delta R/R_0$ gradually increased as the intensity of the applied pressure increased, but the speed tended to be gentle in the high-pressure region. The sensitivity of the pressure sensor (S) was further determined in order to explore the response properties of the sensor more intuitively. One of the important performance parameters of the sensor is sensitively defined as $S = \delta(\Delta R/R_0)/\delta P$ (where $\Delta R/R_0$ and P represent the relative resistance change ratio and the applied pressure, respectively). Similar to most reported pressure sensors, Figure 2C depicts that the pressure responses of this sensor consist of multiple domains.[55] For the pressure sensing, $\Delta R/R_0$ increased rapidly with the pressure increase in the low-pressure range (<2.0 kPa), and the sensitivity of the sensor at this point was 0.115 kPa^{-1}. Then, it gradually slowed down, and the sensitivity reached 0.036 kPa^{-1} from 2.0 to 12 kPa and finally tended to the saturation value in the high-pressure region (>12 kPa), showing that the conductive rGO-C had an excellent conductivity in a network with a wide printing area. The multizone pressure behavior was determined by the structure of the conductive fabric, and the structure change process would be discussed later. In addition, the rGO-C-based multimodal sensor had excellent reliability, long-term stability, and quick response to pressure detection. As illustrated in Figure 2D, by repeatedly loading and unloading different pressures (2.0, 5.0, 8.0, and 10.0 kPa) onto the pressure sensor, it was found that the pressure response maintained almost the same value at one certain pressure, only accompanied by small fluctuations. The relative standard deviations of the relative resistivity changes were 0.95, 1.07, 0.95, and 0.84% corresponding to the applied pressure of 2.0, 5.0, 8.0, and 10.0 kPa, respectively. Such precise and stable sensing behavior indicated the excellent repeatability of the sensor. The response time by applying sudden pressure was further investigated. As shown in Figure 2E, the pressure sensor had a quick response (0.5 s) and recovery time (0.3 s) to meet actual demand. Aiming at further evaluating its stable compression properties, the detection behavior of the sensor was collected in the 250 cycle test of loading−unloading at 1.0 kPa (Figure 2F). During the cycle, the pressure response remained fairly balanced at the start and end points (Figure S7) and there was no apparent variation in the output signal, confirming the durability of the prepared sensor and the potential for long-term use in practical applications. In general, these results sufficiently demonstrated that the multimodal sensor possessed significant sensing performance in detecting pressure.

To realize the sensing mechanism better, Figure 2G reveals the internal structural changes of the rGO-C-based sensor when exposed to external pressure. The rich porous structure of the cotton fabric contributes to the sensitive response behavior at lower pressure. Under the action of pressure, the cross section of the conductive fabric was narrowed and other adjacent conductive fibers were allowed to contact each other to form a conductive path, resulting in a significant decrease in the resistance of the conductive fabric. With the further increase in external pressure, the number of contact points increased further and the conductive network tended to saturate after reaching a certain level. Therefore, the sensitivity was low under high pressure.

3.3. Temperature-Sensing Properties.

rGO—a graphene material synthesized from exfoliated GO by thermal or chemical reductions, has attracted a lot of attention ascribed to an NTC and favorable electrical properties. The resistance (R) at a certain temperature (T) can be expressed by the formula as follows

$$R(T) = R(0) - \left(\frac{\hbar}{e^2}\right)\left(\frac{4TV_0}{\hbar v^2 E_f \tau_0}\right)$$

where $\hbar$ represents the Planck constant, v means the velocity, e is the charge of the electron, E_f and τ_0 are the Fermi energy and the backscattering rate of the atomic sharp defects in the graphene lattice, and V_0 is the characteristic interaction constant.[56] The thermal excitation process of charge carriers in rGO sheets is shown in Figure 3A. With the increase in

https://doi.org/10.1021/acsami.1c16514
ACS Appl. Mater. Interfaces 2021, 13, 46440−46450

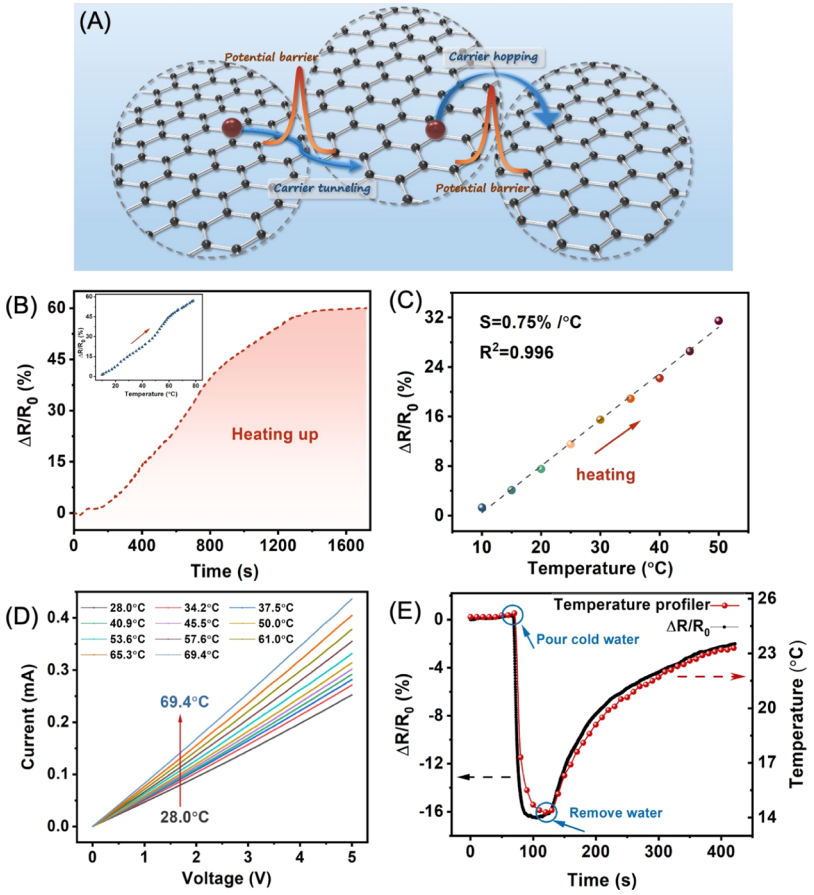

Figure 3. (A) Carrier transport (tunneling and hopping) between neighboring rGO sheets. (B) Response of relative resistance variation with temperature during heating (the illustration corresponds to the temperature change process). (C) Sensitivity of the multimodal sensor for temperature sensing. (D) $I-V$ curves (0−5 V) with different temperatures (28−69.4 °C). (E) Response of the multimodal sensor when pouring cold water into the vial to which the sensor was attached.

thermal energy (at a given temperature), the tunneling and hopping ability of carriers between nanosheets improved in order to have a greater chance of overcoming the potential barrier.[21,57] The increased infinite jumping and tunneling between adjacent rGO sheets leads to a significant increase in the carrier mobility of the conductive film and a decrease in resistance.

Therefore, aiming at evaluating the temperature sensing performance of the rGO-C-based multimodal sensor, the relative resistance variation [$\Delta R/R_0 = (R_0 - R_T)/R_0 \times 100\%$, where R_0 is the initial resistance and R_T equals the resistance of the device when a certain temperature is applied] is introduced as the response level to reflect the sensitive behavior. As displayed in Figure 3B, $\Delta R/R_0$ increased significantly with the increasing temperature, which meant a decrease in resistance. The $\Delta R/R_0-T$ curve shows the generally linear response behavior for the temperature detection with a gradual increase from 10 to 80 °C. Especially at 10−50 °C, $\Delta R/R_0$ and T exhibited an excellent correlation (R^2 = 0.996), and the sensitivity (S, is defined by the formula $S = \Delta R/R_0 \times 1/\Delta T \times 100\%$, where $\Delta R/R_0$ and ΔT represent changes in relative resistance fluctuations and temperature changes) extracted from the linear fit reaches 0.75% per °C (Figure 3C). The $I-V$ curve (Figure 3D) of the sensor was revealed according to the temperature increased from 28 to 69.4 °C (the value of the actual temperature was recorded by the digital thermometer of the sensor surface). At a fixed voltage of 5 V, the current of the temperature sensor increased from 0.25 mA at 28.0 °C to 0.44 mA at 69.4 °C, which clearly shown an NTC property. To additionally verify whether the sensor could effectively detect the surface temperature of the object, the sensor was firmly attached to the wall of the vial and a digital thermometer was attached to the surface of the sensor in order to detect the actual temperature. It could be seen from Figures 3E and S8A that when cold water and hot water were added to the vial, $\Delta R/R_0$ decreased and increased, respectively. The red curve shown in Figure 3E points to the real-time temperature change. It was not difficult to determine that the temperature measured by the sensor matched the change on the digital thermometer and there was no apparent hysteresis. The response time of the temperature sensing was further investigated to 15.5 s (Figure S8B). Although the detection time in this experiment was set to 800 s, there was a certain delay, but it was sufficient to meet the requirements in practical application.

3.4. Feasibility Study of an Enhanced Pressure-Based Immunoassay Platform. The enhanced pressure-based immunoassay was based on the synergistic improvement result of the temperature and pressure. To achieve the design, the sensor must simultaneously monitor the temperature and pressure changes in real time. At this point, an integrated detection device was assembled to install the multimodal sensor to verify the sensing performance (Scheme S1). The platform was crude but useful and provides a reference for

https://doi.org/10.1021/acsami.1c16514
ACS Appl. Mater. Interfaces 2021, 13, 46440−46450

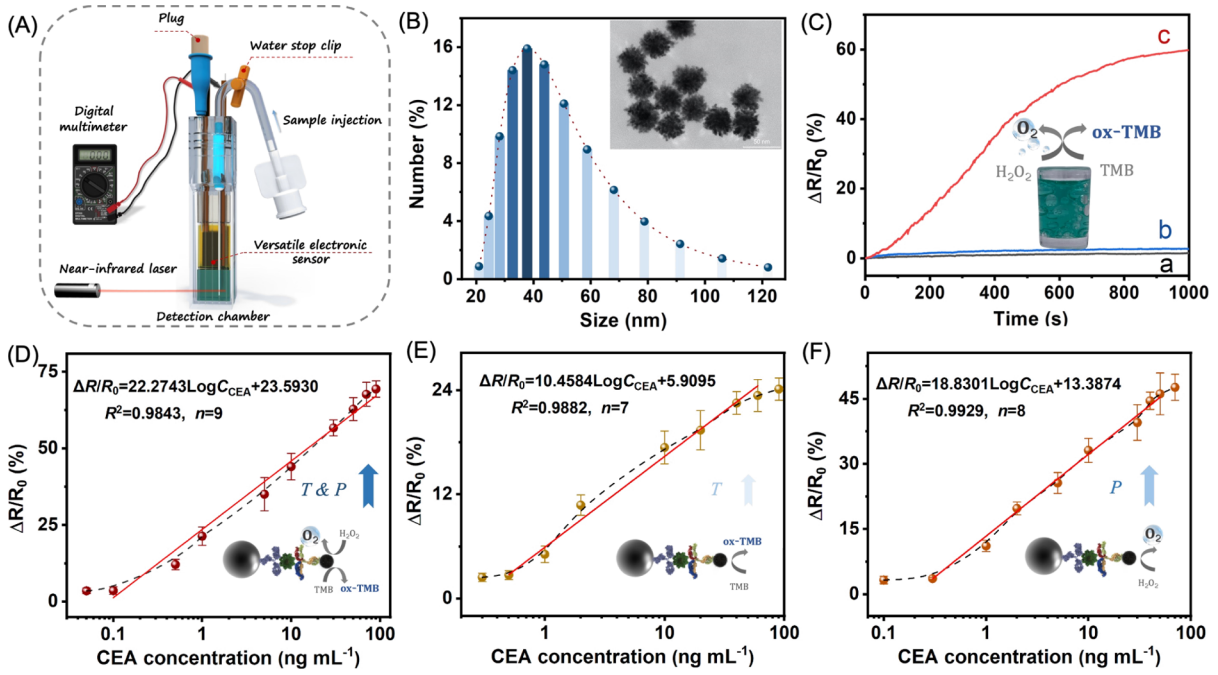

Figure 4. (A) Enhanced pressure-based immunoassay system with the multimodal sensor. (B) Hydrodynamic diameter distribution of PtNPs extracted from DLS measurements and TEM image of the synthesized PtNPs (inset). (C) Signal responses of the immunoassay system (a) without H_2O_2 and target, (b) with H_2O_2, and (c) with H_2O_2 and target. Calibration curve of (D) enhanced pressure-based immunoassay with the synergistic increase in temperature and pressure; (E) immunoassay system took place in an unclosed detection cell (only change in temperature), and (F) immunoassay system without NIR laser irradiation (only change in pressure).

further commercialization (the photographs of the prepared integrated sensing platform are shown in Figure S9). This immunoassay platform mainly consists of a NIR laser, a digital multimeter, and an integrated detection device. Among them, the detailed structure of the detection cell is shown in Figure 4A. The lower part of the detection chamber was the place where the gas and heat generations take place. The inner wall of one side of the detection cell was covered with a thin, thermally conductive layer (Figure S10) for better heat conduction. To illustrate the thermal conductivity, a plastic cuvette covered with thermal grease was placed in a vial with hot water (at about 53 °C) to ensure the hot water dipped the lower part of the thermal interface (Figure S11). Compared to the samples without cover [Figure S11A(a)] and covered with the copper sheet [Figure S11B(b)], the thermally conductive layer displayed excellent thermal conductivity. The temperature of the thermally conductive layer exposed to the air on the top was measured to be 49.7 °C through infrared thermal imaging [Figure S11C(c)]. For pressure-based immunoassay systems, gas production plays an important role in the combination of biometric recognition and signal reading. As a catalyst, PtNPs can promote the decomposition of H_2O_2 to proceed more efficiently and faster, thereby generating a large amount of oxygen in a short period. As demonstrated by the TEM image in Figure 4B, PtNPs of uniform size were successfully synthesized. The rough structure of PtNPs offered plenty of active sites for catalytic reactions. Dynamic light scattering (DLS) also confirmed that the diameters of the synthesized platinum nanoparticles were concentrated around 38 ± 6 nm (Figure 4B). In addition, PtNPs also have peroxidase-like catalytic activity to catalyze TMB into a blue product of oxidized TMB (ox-TMB) in the presence of H_2O_2. The characteristic absorption peak of ox-TMB reached at 652 nm is shown in Figure S12 of the PtNPs−H_2O_2−TMB catalytic system, suggesting that the addition of TMB to the general PtNP-catalyzed H_2O_2 gas generation system could catalyze the simultaneous occurrence of two reactions. As illustrated in the inset of Figure 4C, there appeared a large amount of gas generated in the PtNPs−H_2O_2−TMB system, which could be perceived by bubbles on the wall of a polystyrene 96-well plate, and the solution turned blue at the same time. It was confirmed that ox-TMB was a photothermal agent and caused the temperature of the solution to rise sharply when irradiated with a NIR laser. As shown in Figure S13, the temperature of the solution increased from 25.4 to 50.3 °C from the NIR images within 3 min.

To make the idea a reality, we verified the feasibility of the proposed immunoassay. In this regard, the response was tested in the absence and presence of H_2O_2 and target, respectively. The blank group without H_2O_2 and target (curve a) had almost no signal change (Figure 4C). Also, a weak signal output was observed when adding H_2O_2 (curve b in Figure 4C), which could be caused by partial decomposition of H_2O_2. In contrast, significant signal changes occurred when H_2O_2, TMB, and the target coexisted (curve c in Figure 4C). In order to verify that the presence of two physical quantities of temperature and air pressure could synergize the signal amplification, we compared the use of a single physical quantity only with temperature or air pressure at the same analyte concentration. As shown in Figure S14 (curve a), the "H_2O_2−TMB−CEA" system showed the signal output based on temperature changes when irradiated with a NIR laser in an unclosed detection cell. At this point in time, the value of $\Delta R/R_0$ was 18.05%. The curve b shown in Figure S14 shows the output signal curve of the "H_2O_2−TMB−CEA" system without NIR laser irradiation. At this point, only the change in air pressure affected the sensor, and it was seen that the signal output reached the plateau value when $\Delta R/R_0$ was

https://doi.org/10.1021/acsami.1c16514
ACS Appl. Mater. Interfaces 2021, 13, 46440−46450

39.02%. It could be clearly seen that the dual physical quantity had a synergistic amplification effect on the signal output and that the signal intensity ($\Delta R/R_0 \approx 56.96\%$) increased approximately 3.16 times (T) and 1.46 times (P), if a single physical quantity existed (the curve c in Figure S14). Therefore, with the help of PtNP-labeling strategies, we were able to clearly demonstrate that the versatile electronic sensor can be used for an enhanced pressure-based immunoassay based on the dual physical quantities of temperature and air pressure.

3.5. Analytical Performance of Enhanced Pressure-Based Immunoassay. To justify the highly sensitive detection performance, some important influencing factors must be optimized. As shown in Figure S15, the H_2O_2 concentration, the TMB concentration, and the catalytic reaction time were explored as three key points. Under the optimal reaction conditions, at a concentration of 30% H_2O_2 mixed with 5 mM TMB, the signal response was recorded with a catalysis time of 800 s. By measuring the signal output of the target CEA at different concentrations under optimal conditions, the dynamic working range of the enhanced pressure-based immunoassay for CEA could easily be achieved from 0.1 to 90 ng mL^{-1}. As shown in Figure 4D that the linear equation was $\Delta R/R_0 = 22.2743 \log C_{CEA} + 23.5930$ ($R^2 = 0.9843$, $n = 9$) resulting in a limit of detection (LOD) of 81 pg mL^{-1} (obtained from $3\sigma/K$, where σ and K were the standard deviation of 11 blank groups and the slope of the calibration plot, respectively). It was noteworthy that we examined the detection system with only changes in temperature or air pressure to compare the difference between the designed enhanced pressure-based immunoassay in the analytical performance of the target with only a single physical variable. If only the temperature changed significantly and the pressure value remained roughly unchanged (the reaction happened in an unclosed detection cell), then the CEA concentration from 0.5 to 40 ng mL^{-1} (Figure 4E) corresponded to a linear increase in the value of $\Delta R/R_0$ and satisfies the equation $\Delta R/R_0 = 10.4584 \log C_{CEA} + 5.9095$ ($R^2 = 0.9882$, $n = 7$). When the laser was removed from the detection system, the temperature increase of the solution was not visible and the response signal was mainly caused by the significant change in the air pressure in the closed device. As shown in Figure 4F, the output $\Delta R/R_0$ was directly proportional to the CEA concentration in the range of 0.3−50 ng mL^{-1} with a quadratic correlation coefficient (R^2) of 0.9929 ($\Delta R/R_0 = 18.8301 \log C_{CEA} + 13.3874$, $n = 8$). It was not difficult to see that the enhanced pressure-based immunoassay developed in this experiment, which was influenced by both temperature and pressure, showed better detection performance and the potential to meet the requirements of clinical detection. To further clarify the significance and novelty of the proposed immunoassay, some of our previous works for CEA detection are summarized in Table S3. In general, the advantages and breakthroughs can be summarized as follows: (i) a new type of sensor based on different signal translation principles was put into use, which was utilized for the first conceptual verification to simultaneously monitor the changes of two physical quantities produced in the immunoassay process; (ii) different from simple pressure sensors, the use of multimodal sensors broadened the diversity of flexible sensors in biological analysis applications and provided ideas for exploring more multi-dimensional and intelligent point-of-care settings; (iii) the integrated detection device combined signal generation and detection parts to avoid detection errors caused by the gas leakage or gas stagnation in the connecting pipe and the repeated plugging and unplugging of the sensor in the combination detection device; and (iv) a wider linear range and lower LOD were obtained compared with other methods. Unfortunately, the progress was not a quantum leap. However, based on the conceptual verification of the proposed immunoassay model, we believed that under the long exploration of more high-performance multimodal sensors, immunoassays with excellent detection performance can be developed. Furthermore, the analytical properties of the proposed strategy were compared with other previously published methods for CEA detection (Table S4). Obviously, depending on expensive instruments and professional operations, some CEA biosensors obtained a quite low LODs. Especially compared with photoelectrochemical and electrochemical immunoassays, the sensitivity of this work was lower than these. However, our method got rid of the shackles of large instruments, thus achieving simpler readout and more portable detection. Such a strategy was beneficial for its applications in situations with limited equipment such as homes or on-site. As a portable detection method, considerable analytical performance was achieved in our immunoassay to meet the requirements of practical applications.

To investigate the specificity of the enhanced pressure-based immunoassay based on the target CEA, several common human tumor markers in the blood (such as AFP, PSA, and IgG) were tested as interfering analytes. As depicted in Figure 5, these high concentrations of nontarget tumor markers compared to the blank control group (without analytes) only led to a relatively low signal response, while with the target CEA alone or the CEA-containing mixture resulted in a significant signal change. These results prove that the enhanced pressure-based immunoassay based on multimodal sensors has a high specificity even with high concentrations of interfering substances.

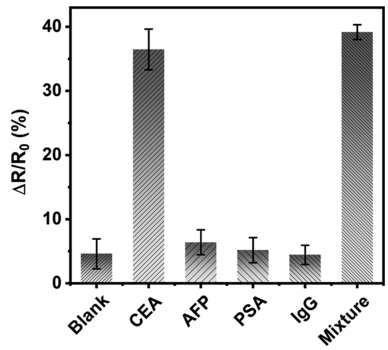

Figure 5. Selectivity of the proposed enhanced pressure-based immunoassay.

To further evaluate the possibility of the proposed immunoassay model in practical applications, six fresh blood samples were measured (the blood samples were from the Fujian Mengchao Hepatobiliary Hospital). Typically, the threshold value of CEA in healthy human serum is about 3 ng mL^{-1}. The criteria for the CEA detection of human serum specimens are to determine clinically positive ($C_{[CEA]} \geq 3$ ng mL^{-1}) and clinically negative ($C_{[CEA]} < 3$ ng mL^{-1}) results. The t-test was used for the statistical analysis of the results obtained by the two methods of the proposed immunoassay

https://doi.org/10.1021/acsami.1c16514
ACS Appl. Mater. Interfaces 2021, 13, 46440−46450

and the commercial CEA ELISA kit (Table 1). It was worth noting that all the maximum t_{exp} (t-experimental) values in these cases were $<t_{crit[0.05,4]}$ (t-critical, $t_{crit[0.05,4]}$ = 2.78). In addition, there also existed a good linear relationship (R^2 = 0.988) between the two methods with a slope close to "1" and the intercept nearby "0" (Figure S16). Comparison of the abovementioned test results shows that the enhanced pressure-based immunoassay is acceptable for the detection accuracy of CEA and can be expected to be used initially for the practical detection of biological samples.

Table 1. Accuracy Assessment for Human Serum Specimens between the Enhanced Pressure-Based Immunoassay and the Commercial Human CEA ELISA Kit

	method accuracy (conc.: mean ± SD, ng mL $^{-1}$, n = 3)[a]		
sample no.	enhanced pressure-based immunoassay	CEA ELISA kit	t_{exp}
1	37.58 ± 1.94	34.59 ± 1.36	2.19
2	22.28 ± 3.01	23.76 ± 1.00	0.81
3	18.18 ± 1.37	16.03 ± 1.47	1.85
4	26.78 ± 3.07	27.16 ± 2.28	0.17
5	5.12 ± 0.44	5.49 ± 0.57	0.89
6	7.76 ± 1.58	9.31 ± 0.73	1.54
7	1.22 ± 0.09	1.01 ± 0.11	2.56
8	0.15 ± 0.06	0.18 ± 0.03	0.77

[a]Each sample was determined in triplicate, and the high-concentration CEA samples were appropriately diluted.

4. CONCLUSIONS

In summary, as a proof of concept, we successfully demonstrated an enhanced pressure-based immunoassay that implements a signal amplification method based on the dual physical quantities of temperature and air pressure. Compared to the general pressure-based immunoassays, this method is advantageous because it acts on the versatile electronic sensor through a triple-step signal amplification strategy of pressure increase, temperature increase, and gas thermal expansion, which provides a portable, widely useful, and highly sensitive biosensing platform. We expect that the chemomechanical signal transduction principle will significantly expand the potential of flexible electronic sensors in the development of innovative biomedical assays by using versatile electronic sensors for the simultaneous detection of multiple physical quantities. Moreover, we envision that such multimodal devices have the potential to create a handheld bioassay that can monitor electrophysiological, physical, and chemical signals and enable the development of a portable, low-cost, and instant diagnosis in clinical settings.

ASSOCIATED CONTENT

Supporting Information

The Supporting Information is available free of charge at https://pubs.acs.org/doi/10.1021/acsami.1c16514.

Materials and reagents; apparatus; preparation of GO, platinum nanoparticles, platinum nanoparticle-labeled detection antibodies and magnetic beads-labeled capture antibodies; immunoassay procedure; characterization; and optimization of experimental conditions (PDF)

AUTHOR INFORMATION

Corresponding Author

Dianping Tang − *Key Laboratory of Analytical Science for Food Safety and Biology (MOE & Fujian Province), Department of Chemistry, Fuzhou University, Fuzhou 350108, P. R. China; Chongqing Vocational Institute of Engineering, Chongqing 402260, P. R. China;* orcid.org/0000-0002-0134-3983; Phone: +86-591-2286 6125; Email: dianping.tang@fzu.edu.cn; Fax: +86-591-2286 6135

Authors

Lingting Huang − *Key Laboratory of Analytical Science for Food Safety and Biology (MOE & Fujian Province), Department of Chemistry, Fuzhou University, Fuzhou 350108, P. R. China*

Yongyi Zeng − *The United Innovation of Mengchao Hepatobiliary Technology Key Laboratory of Fujian Province, Mengchao Hepatobiliary Hospital of Fujian Medical University, Fuzhou 350025, P. R. China*

Xiaolong Liu − *The United Innovation of Mengchao Hepatobiliary Technology Key Laboratory of Fujian Province, Mengchao Hepatobiliary Hospital of Fujian Medical University, Fuzhou 350025, P. R. China;* orcid.org/0000-0002-3096-4981

Complete contact information is available at: https://pubs.acs.org/10.1021/acsami.1c16514

Notes

The authors declare no competing financial interest.

All the experiments were performed in accordance with the Guidelines of Fuzhou University (China) and approved by the ethics committee at Fuzhou University. Informed consent was for any experimentation with human subjects.

ACKNOWLEDGMENTS

Authors acknowledged financial support from the National Natural Science Foundation of China (grant nos. 21874022 and 21675029) and the Natural Science Foundation of Chongqing (grant no. cstc2020jcyj-msxmX0977).

REFERENCES

(1) Bates, S. E. Clinical-Applications of Serum Tumor-Markers. *Ann. Intern. Med.* **1991**, *115*, 623−638.

(2) Swierczewska, M.; Liu, G.; Lee, S.; Chen, X. High-sensitivity Nanosensors for Biomarker detection. *Chem. Soc. Rev.* **2012**, *41*, 2641−2655.

(3) Xu, Z.; Liu, Z.; Xiao, M.; Jiang, L.; Yi, C. A Smartphone-based Quantitative Point-of-care Testing (POCT) System for Simultaneous Detection of Multiple Heavy Metal Ions. *Chem. Eng. J.* **2020**, *394*, 124966.

(4) Yang, M.; Liu, Y.; Jiang, X. Barcoded Point-of-care Bioassays. *Chem. Soc. Rev.* **2019**, *48*, 850−884.

(5) Shrivastava, S.; Trung, T. Q.; Lee, N.-E. Recent Progress, Challenges, and Prospects of Fully Integrated Mobile and Wearable Point-of-care Testing Systems for Self-testing. *Chem. Soc. Rev.* **2020**, *49*, 1812−1866.

(6) Xu, H.; Xia, A.; Wang, D.; Zhang, Y.; Deng, S.; Lu, W.; Luo, J.; Zhong, Q.; Zhang, F.; Zhou, L.; Zhang, W.; Wang, Y.; Yang, C.; Chang, K.; Fu, W.; Cui, J.; Gan, M.; Luo, D.; Chen, M. An Ultraportable and Versatile Point-of-care DNA Testing Platform. *Sci. Adv.* **2020**, *6*, No. eaaz7445.

(7) Williams, N. X.; Carroll, B.; Noyce, S. G.; Hobbie, H. A.; Joh, D. Y.; Rogers, J. G.; Franklin, A. D. Fully Printed Prothrombin Time

Sensor for Point-of-care Testing. *Biosens. Bioelectron.* **2021**, *172*, 112770.
(8) Zhu, Z.; Guan, Z.; Jia, S.; Lei, Z.; Lin, S.; Zhang, H.; Ma, Y.; Tian, Z. Q.; Yang, C. J. Au@Pt Nanoparticle Encapsulated Target-Responsive Hydrogel with Volumetric Bar-Chart Chip Readout for Quantitative Point-of-Care Testing. *Angew. Chem. Int. Ed.* **2014**, *53*, 12503−12507.
(9) Zeng, R.; Tao, J.; Tang, D.; Knopp, D.; Shu, J.; Cao, X. Biometric-based Tactile Chemomechanical Transduction: An Adaptable Strategy for Portable Bioassay. *Nano Energy* **2020**, *71*, 104580.
(10) Yu, Z.; Cai, G.; Liu, X.; Tang, D. Platinum Nanozyme-Triggered Pressure-Based Immunoassay Using a Three-Dimensional Polypyrrole Foam-Based Flexible Pressure Sensor. *ACS Appl. Mater. Interfaces* **2020**, *12*, 40133−40140.
(11) Lv, S.; Zhang, K.; Tang, D. A New Visual Immunoassay for Prostate-specific Antigen Using Near-infrared Excited CuxS Nanocrystals and Imaging on a Smartphone. *Analyst* **2019**, *144*, 3716−3720.
(12) He, R.; Niu, Y.; Li, Z.; Li, A.; Yang, H.; Xu, F.; Li, F. A Hydrogel Microneedle Patch for Point-of-Care Testing Based on Skin Interstitial Fluid. *Adv. Healthcare Mater.* **2020**, *9*, 1901201.
(13) Zhu, Z.; Guan, Z.; Liu, D.; Jia, S.; Li, J.; Lei, Z.; Lin, S.; Ji, T.; Tian, Z.; Yang, C. J. Translating Molecular Recognition into a Pressure Signal to enable Rapid, Sensitive, and Portable Biomedical Analysis. *Angew. Chem., Int. Ed.* **2015**, *54*, 10448−10453.
(14) Yu, Z.; Cai, G.; Liu, X.; Tang, D. Pressure-Based Biosensor Integrated with a Flexible Pressure Sensor and an Electrochromic Device for Visual Detection. *Anal. Chem.* **2021**, *93*, 2916−2925.
(15) Huang, L.; Yu, Z.; Chen, J.; Tang, D. Pressure-Based Bioassay Perceived by a Flexible Pressure Sensor with Synergistic Enhancement of the Photothermal Effect. *ACS Appl. Bio Mater.* **2020**, *3*, 9156−9163.
(16) Zeng, R.; Wang, W.; Chen, M.; Wan, Q.; Wang, C.; Knopp, D.; Tang, D. CRISPR-Cas12a-driven MXene-PEDOT:PSS Piezoresistive Wireless Biosensor. *Nano Energy* **2021**, *82*, 105711.
(17) Lu, Y.; Xu, K.; Zhang, L.; Deguchi, M.; Shishido, H.; Arie, T.; Pan, R.; Hayashi, A.; Shen, L.; Akita, S.; Takei, K. Multimodal Plant Healthcare Flexible Sensor System. *ACS Nano* **2020**, *14*, 10966−10975.
(18) Jeon, S.; Lim, S.-C.; Trung, T. Q.; Jung, M.; Lee, N.-E. Flexible Multimodal Sensors for Electronic Skin: Principle, Materials, Device, Array Architecture, and Data Acquisition Method. *Proc. IEEE* **2019**, *107*, 2065−2083.
(19) Kweon, O. Y.; Samanta, S. K.; Won, Y.; Yoo, J. H.; Oh, J. H. Stretchable and Self-Healable Conductive Hydrogels for Wearable Multimodal Touch Sensors with Thermoresponsive Behavior. *ACS Appl. Mater. Interfaces* **2019**, *11*, 26134−26143.
(20) Wu, Q.; Qiao, Y.; Guo, R.; Naveed, S.; Hirtz, T.; Li, X.; Fu, Y.; Wei, Y.; Deng, G.; Yang, Y.; Wu, X.; Ren, T.-L. Triode-Mimicking Graphene Pressure Sensor with Positive Resistance Variation for Physiology and Motion Monitoring. *ACS Nano* **2020**, *14*, 10104−10114.
(21) Trung, T. Q.; Ramasundaram, S.; Hwang, B.-U.; Lee, N.-E. An All-Elastomeric Transparent and Stretchable Temperature Sensor for Body-Attachable Wearable Electronics. *Adv. Mater.* **2016**, *28*, 502−509.
(22) Georgakilas, V.; Perman, J. A.; Tucek, J.; Zboril, R. Broad Family of Carbon Nanoallotropes: Classification, Chemistry, and Applications of Fullerenes, Carbon Dots, Nanotubes, Graphene, Nanodiamonds, and Combined Superstructures. *Chem. Rev.* **2015**, *115*, 4744−4822.
(23) Zheng, S.; Jiang, Y.; Wu, X.; Xu, Z.; Liu, Z.; Yang, W.; Yang, M. Highly Sensitive Pressure Sensor with Broad Linearity Via Constructing a Hollow Structure in Polyaniline/polydimethylsiloxane Composite. *Compos. Sci. Technol.* **2021**, *201*, 108546.
(24) Wang, Y.; Mao, H.; Wang, Y.; Zhu, P.; Liu, C.; Deng, Y. 3D Geometrically Structured PANI/CNT-decorated Polydimethylsiloxane Active Pressure and Temperature Dual-parameter Sensors for Man-machine Interaction Applications. *J. Mater. Chem. A* **2020**, *8*, 15167−15176.
(25) Ren, X.; Pei, K.; Peng, B.; Zhang, Z.; Wang, Z.; Wang, X.; Chan, P. K. L. A Low-Operating-Power and Flexible Active-Matrix Organic-Transistor Temperature-Sensor Array. *Adv. Mater.* **2016**, *28*, 4832−4838.
(26) Peng, S.; Wu, S.; Yu, Y.; Xia, B.; Lovell, N. H.; Wang, C. H. Multimodal Capacitive and Piezoresistive Sensor for Simultaneous Measurement of Multiple Forces. *ACS Appl. Mater. Interfaces* **2020**, *12*, 22179−22190.
(27) Guan, F.; Xie, Y.; Wu, H.; Meng, Y.; Shi, Y.; Gao, M.; Zhang, Z.; Chen, S.; Chen, Y.; Wang, H.; Pei, Q. Silver Nanowire-Bacterial Cellulose Composite Fiber-Based Sensor for Highly Sensitive Detection of Pressure and Proximity. *ACS Nano* **2020**, *14*, 15428−15439.
(28) Gong, S.; Schwalb, W.; Wang, Y.; Chen, Y.; Tang, Y.; Si, J.; Shirinzadeh, B.; Cheng, W. A Wearable and Highly Sensitive Pressure Sensor with Ultrathin Gold Nanowires. *Nat. Commun.* **2014**, *5*, 3132.
(29) Chen, H.; Su, Z.; Song, Y.; Cheng, X.; Chen, X.; Meng, B.; Song, Z.; Chen, D.; Zhang, H. Omnidirectional Bending and Pressure Sensor Based on Stretchable CNT-PU Sponge. *Adv. Funct. Mater.* **2017**, *27*, 1604434.
(30) Kim, J.-H.; Kim, S.-R.; Kil, H.-J.; Kim, Y.-C.; Park, J.-W. Highly Conformable, Transparent Electrodes for Epidermal Electronics. *Nano Lett.* **2018**, *18*, 4531−4540.
(31) Tao, L.-Q.; Zhang, K.-N.; Tian, H.; Liu, Y.; Wang, D.-Y.; Chen, Y.-Q.; Yang, Y.; Ren, T.-L. Graphene-Paper Pressure Sensor for Detecting Human Motions. *ACS Nano* **2017**, *11*, 8790−8795.
(32) Xiong, J.; Lin, M.-F.; Wang, J.; Gaw, S. L.; Parida, K.; Lee, P. S. Wearable All-Fabric-Based Triboelectric Generator for Water Energy Harvesting. *Adv. Energy Mater.* **2017**, *7*, 1701243.
(33) Qi, K.; Wang, H.; You, X.; Tao, X.; Li, M.; Zhou, Y.; Zhang, Y.; He, J.; Shao, W.; Cui, S. Core-sheath Nanofiber Yarn for Textile Pressure Sensor with High Pressure Sensitivity and Spatial Tactile Acuity. *J. Colloid Interface Sci.* **2020**, *561*, 93−103.
(34) Gao, Y.; Yu, L.; Yeo, J. C.; Lim, C. T. Flexible Hybrid Sensors for Health Monitoring: Materials and Mechanisms to Render Wearability. *Adv. Mater.* **2020**, *32*, 1902133.
(35) Kabiri Ameri, S.; Ho, R.; Jang, H.; Tao, L.; Wang, Y.; Wang, L.; Schnyer, D. M.; Akinwande, D.; Lu, N. Graphene Electronic Tattoo Sensors. *ACS Nano* **2017**, *11*, 7634−7641.
(36) Feng, S.; Li, Q.; Wang, S.; Wang, B.; Hou, Y.; Zhang, T. Tunable Dual Temperature-Pressure Sensing and Parameter Self-Separating Based on Ionic Hydrogel via Multisynergistic Network Design. *ACS Appl. Mater. Interfaces* **2019**, *11*, 21049−21057.
(37) Zu, G.; Kanamori, K.; Nakanishi, K.; Huang, J. Superhydrophobic Ultraflexible Triple-Network Graphene/Polyorganosiloxane Aerogels for a High-Performance Multifunctional Temperature/Strain/Pressure Sensing Array. *Chem. Mater.* **2019**, *31*, 6276−6285.
(38) Li, Q.; Zhang, L. N.; Tao, X. M.; Ding, X. Review of Flexible Temperature Sensing Networks for Wearable Physiological Monitoring. *Adv. Healthcare Mater.* **2017**, *6*, 1601371.
(39) Maria Joseph Raj, N. P.; Alluri, N. R.; Khandelwal, G.; Kim, S.-J. Lead-free Piezoelectric Nanogenerator Using Lightweight Composite Films for Harnessing Biomechanical Energy. *Composites, Part B* **2019**, *161*, 608−616.
(40) Arman Kuzubasoglu, B.; Kursun Bahadir, S. Flexible Temperature Sensors: A Review. *Sens. Actuators, A* **2020**, *315*, 112282.
(41) Cui, Z.; Poblete, F. R.; Zhu, Y. Tailoring the Temperature Coefficient of Resistance of Silver Nanowire Nanocomposites and their Application as Stretchable Temperature Sensors. *ACS Appl. Mater. Interfaces* **2019**, *11*, 17836−17842.
(42) Hong, S. Y.; Lee, Y. H.; Park, H.; Jin, S. W.; Jeong, Y. R.; Yun, J.; You, I.; Zi, G.; Ha, J. S. Stretchable Active Matrix Temperature Sensor Array of Polyaniline Nanofibers for Electronic Skin. *Adv. Mater.* **2016**, *28*, 930−935.

https://doi.org/10.1021/acsami.1c16514
ACS Appl. Mater. Interfaces 2021, 13, 46440−46450

(43) Chen, J.-H.; Jang, C.; Xiao, S.; Ishigami, M.; Fuhrer, M. S. Intrinsic and Extrinsic Performance Limits of Graphene Devices on SiO_2. *Nat. Nanotechnol.* **2008**, *3*, 206−209.
(44) Al-Mumen, H.; Rao, F.; Dong, L.; Li, W. Thermo-flow and Temperature Sensing Behaviour of Graphene Based on Surface Heat Convection. *Micro Nano Lett.* **2013**, *8*, 681−685.
(45) Dan, L.; Elias, A. L. Flexible and Stretchable Temperature Sensors Fabricated Using Solution-Processable Conductive Polymer Composites. *Adv. Healthcare Mater.* **2020**, *9*, 2000380.
(46) Gao, L.; Zhu, C.; Li, L.; Zhang, C.; Liu, J.; Yu, H.-D.; Huang, W. All Paper-Based Flexible and Wearable Piezoresistive Pressure Sensor. *ACS Appl. Mater. Interfaces* **2019**, *11*, 25034−25042.
(47) Li, C.-Y.; Cao, D.; Qi, C.-B.; Chen, H.-L.; Wan, Y.-T.; Lin, Y.; Zhang, Z.-L.; Pang, D.-W.; Tang, H.-W. One-step Separation-free Detection of Carcinoembryonic Antigen in Whole Serum: Combination of Two-photon Excitation Fluorescence and Optical Trapping. *Biosens. Bioelectron.* **2017**, *90*, 146−152.
(48) Hummers, W. S.; Offeman, R. E. Preparation of Graphitic Oxide. *J. Am. Chem. Soc.* **1958**, *80*, 1339.
(49) NeeIla, N.; Gaddam, V.; Nayak, M.; Dinesh, N.; Rajanna, K. Scalable Fabrication of Highly Sensitive Flexible Temperature Sensors Based on Silver Nanoparticles Coated Reduced Graphene Oxide Nanocomposite Thin Films. *Sens. Actuators, A* **2017**, *268*, 173−182.
(50) Sehrawat, P.; Abid, A.; Islam, S. S.; Mishra, P. Reduced Graphene Oxide Based Temperature Sensor: Extraordinary Performance Governed by Lattice Dynamics Assisted Carrier Transport. *Sens. Actuators, B* **2018**, *258*, 424−435.
(51) Yang, Z.; Pang, Y.; Han, X.-l.; Yang, Y.; Ling, J.; Jian, M.; Zhang, Y.; Yang, Y.; Ren, T.-L. Graphene Textile Strain Sensor with Negative Resistance Variation for Human Motion Detection. *ACS Nano* **2018**, *12*, 9134−9141.
(52) Sadasivuni, K. K.; Kafy, A.; Kim, H.-C.; Ko, H.-U.; Mun, S.; Kim, J. Reduced Graphene Oxide Filled Cellulose Films for Flexible Temperature Sensor Application. *Synth. Met.* **2015**, *206*, 154−161.
(53) Xu, L.-L.; Guo, M.-X.; Liu, S.; Bian, S.-W. Graphene/cotton Composite Fabrics as Flexible Electrode Materials for Electrochemical Capacitors. *RSC Adv.* **2015**, *5*, 25244−25249.
(54) Tian, M.; Hu, X.; Qu, L.; Zhu, S.; Sun, Y.; Han, G. Versatile and Ductile Cotton Fabric Achieved Via Layer-by-layer Self-assembly by Consecutive Adsorption of Graphene Doped PEDOT: PSS and Chitosan. *Carbon* **2016**, *96*, 1166−1174.
(55) Lee, S.; Reuveny, A.; Reeder, J.; Lee, S.; Jin, H.; Liu, Q.; Yokota, T.; Sekitani, T.; Isoyama, T.; Abe, Y.; Suo, Z.; Someya, T. A Transparent Bending-insensitive Pressure Sensor. *Nat. Nanotechnol.* **2016**, *11*, 472−478.
(56) Sabaté, N.; Santander, J.; Fonseca, L.; Gràcia, I.; Cané, C. Multi-range Silicon Micromachined Flow Sensor. *Sens. Actuators, A* **2004**, *110*, 282−288.
(57) Kobayashi, T.; Kimura, N.; Chi, J.; Hirata, S.; Hobara, D. Channel-Length-Dependent Field-Effect Mobility and Carrier Concentration of Reduced Graphene Oxide Thin-Film Transistors. *Small* **2010**, *6*, 1210−1215.

https://doi.org/10.1021/acsami.1c16514
ACS Appl. Mater. Interfaces 2021, 13, 46440−46450